



# Nonlinear Decay of Alfvén Waves Driven by Interplaying Two- and Three-dimensional Nonlinear Interactions

J. S. Zhao<sup>1,2</sup>, Y. Voitenko<sup>3</sup>, J. De Keyser<sup>3</sup>, and D. J. Wu<sup>1</sup>

<sup>1</sup> Key Laboratory of Planetary Sciences, Purple Mountain Observatory, Chinese Academy of Sciences, Nanjing 210008, People's Republic of China; [js\\_zhao@pmo.ac.cn](mailto:js_zhao@pmo.ac.cn)

<sup>2</sup> CAS Key Laboratory of Solar Activity, National Astronomical Observatories, Beijing 100012, People's Republic of China

<sup>3</sup> Solar-Terrestrial Centre of Excellence, Space Physics Division, Belgian Institute for Space Aeronomy, Avenue Circulaire 3, B-1180 Brussels, Belgium  
Received 2017 August 19; revised 2018 March 1; accepted 2018 March 6; published 2018 April 11

## Abstract

We study the decay of Alfvén waves in the solar wind, accounting for the joint operation of two-dimensional (2D) scalar and three-dimensional (3D) vector nonlinear interactions between Alfvén and slow waves. These interactions have previously been studied separately in long- and short-wavelength limits where they lead to 2D scalar and 3D vector decays, correspondingly. The joined action of the scalar and vector interactions shifts the transition between 2D and 3D decays to significantly smaller wavenumbers than was predicted by Zhao et al. who compared separate scalar and vector decays. In application to the broadband Alfvén waves in the solar wind, this means that the vector nonlinear coupling dominates in the extended wavenumber range  $5 \times 10^{-4} \lesssim \rho_i k_{0\perp} \lesssim 1$ , where the decay is essentially 3D and nonlocal, generating product Alfvén and slow waves around the ion gyroscale. Here  $\rho_i$  is the ion gyroradius, and  $k_{0\perp}$  is the pump Alfvén wavenumber. It appears that, except for the smallest wavenumbers at and below  $\rho_i k_{0\perp} \sim 10^{-4}$  in Channel I, the nonlinear decay of magnetohydrodynamic Alfvén waves propagating from the Sun is nonlocal and cannot generate counter-propagating Alfvén waves with similar scales needed for the turbulent cascade. Evaluation of the nonlinear frequency shift shows that product Alfvén waves can still be approximately described as normal Alfvénic eigenmodes. On the contrary, nonlinearly driven slow waves deviate considerably from normal modes and are therefore difficult to identify on the basis of their phase velocities and/or polarization.

*Key words:* instabilities – magnetohydrodynamics (MHD) – plasmas – solar wind – waves

## 1. Introduction

Alfvén waves observed in the solar atmosphere and solar wind (e.g., McIntosh et al. 2011; Morton et al. 2015; Li et al. 2016b; Yang et al. 2016) are believed to play a significant role in heating the solar corona and accelerating the solar wind (e.g., Asgari-Targhi et al. 2013; van Ballegoijen & Asgari-Targhi 2016). It is important to understand how magnetohydrodynamic (MHD) Alfvén waves dissipate their energy traveling over long distances throughout the solar atmosphere and solar wind.

Inhomogeneity of the Alfvén velocity transverse to the ambient magnetic field in the solar atmosphere can trigger dissipation of Alfvén waves via resonant absorption and phase mixing (Heyvaerts & Priest 1983; Goossens et al. 2011; McLaughlin et al. 2011). On the other hand, a fraction of the upward-propagating Alfvén waves can be reflected back by the inhomogeneity along the ambient magnetic field. The reflected downward-propagating waves can interact nonlinearly with the original upward waves, initiating the turbulent cascade and Alfvénic turbulence (e.g., Matthaeus et al. 1999; Schekochihin et al. 2009; Zhao et al. 2013). When the turbulent cascade reaches sufficiently small scales, Alfvén waves are damped collisionally and/or kinetically to energize plasma particles (e.g., Voitenko & Goossens 2004; Verdini & Velli 2007; Voitenko & De Keyser 2011; TenBarge et al. 2013; He et al. 2015b).

Alfvén waves can be excited through convective motions below the photosphere and/or through changes of the magnetic-field topology in the lower corona (McKenzie et al. 1995; Cranmer & van Ballegoijen 2005; Isobe et al. 2008).

When these waves propagate away from the Sun, their amplitudes increase with radial distance, and can eventually trigger the nonlinear decay instability to produce slow waves (Suzuki & Inutsuka 2005, 2006; Matsumoto & Suzuki 2012; Tenerani & Velli 2013; Shi et al. 2017). The produced slow waves can further form shocks, heating plasma and accelerating particles in the solar atmosphere and solar wind (Del Zanna et al. 2001; Suzuki & Inutsuka 2005).

Nonlinear decay of finite-amplitude Alfvén waves has been investigated extensively in the past both analytically and numerically (e.g., Galeev & Oraevskii 1963; Barnes & Hollweg 1974; Vasquez & Hollweg 1996; Del Zanna 2001; Matteini et al. 2010a, 2010b; Tenerani & Velli 2013; Del Zanna et al. 2015). Results of these studies have been used to explain the wave damping and related phenomena in the solar corona and solar wind. However, the nature of the decay and its efficiency are still not fully understood, especially for oblique waves that are common in solar and space plasmas. A promising progress in this direction includes, in particular, the recent finding that in different wavenumber ranges different scalar- and vector-type nonlinear forces dominate the nonlinear coupling between Alfvén and slow waves (Zhao et al. 2014, 2015a). The nonlinear decay modified by the vector nonlinear effects has recently been proposed as an efficient damping mechanism for Alfvén waves with periods  $\sim 100$  s and transverse wavelengths  $\lesssim 10^4$  km in polar coronal holes (Zhao et al. 2015b), providing a feasible explanation for the damping of Alfvén waves observed at  $\lesssim 1.5$  solar radii (Bemporad & Abbo 2012; Hahn et al. 2012). Alfvén waves propagating toward the Sun can be produced by the nonlinear decay and/or by the reflection of outward Alfvén waves off the local density

inhomogeneities due to compressive waves (Suzuki & Inutsuka 2005; Shoda & Yokoyama 2016). This may cause the observed cross-helicity decrease with the radial distance in the solar wind (Del Zanna et al. 2015).

When all interacting Alfvén and slow waves have MHD scales, the nonlinear forces  $\propto n\partial_t \mathbf{v}_\perp$  and  $\propto \mathbf{B}_\perp \cdot \mathbf{B}_\perp$  drive the nonlinear current density and nonlinear pressure, respectively. Here  $n$  is the number density perturbation due to the slow wave, whereas  $\mathbf{B}_\perp$  and  $\mathbf{v}_\perp$  are the magnetic field and velocity perturbations due to the MHD Alfvén wave. Under the action of these forces, a forward pump Alfvén wave decays into a backward Alfvén wave and a forward slow wave, which was originally studied by Galeev & Oraevskii (1963), followed by, e.g., Goldstein (1978) and many others. We denote this decay channel as Channel I.

If the pump Alfvén wave is still MHD, but the product waves are not restricted to be MHD, we have to use at least a two-fluid MHD model. In this case, the perpendicular wavelengths of the product waves can extend from the MHD down to ion kinetic scales (Matteini et al. 2010a; Zhao et al. 2014). The product Alfvén wave is driven by the same nonlinear force as in the MHD case, but the slow wave is now driven by a combination of the nonlinear Lorentz force  $\propto e(\mathbf{v}_{iA} \times \mathbf{B}_\perp) \cdot \hat{\mathbf{z}}$  and the nonlinear inertial force  $\propto m_i \mathbf{v}_{iA} \cdot \nabla_\perp \mathbf{v}_{iA}$ . Here  $\mathbf{v}_{iA}$  and  $\mathbf{v}_{iA}$  are the ion velocities driven by Alfvén waves (subscript A) in the directions  $\hat{\mathbf{e}}_t \equiv \mathbf{k}_\perp / k_\perp$  and  $\hat{\mathbf{z}} \equiv \mathbf{B}_0 / B_0$ ,  $\mathbf{k}_\perp$  is the perpendicular wavevector of the pump Alfvén wave, and  $\mathbf{B}_0$  is the ambient magnetic field. In addition to the Channel I decay, the MHD Alfvén wave can now decay into the kinetic-scale forward Alfvén and slow waves (Zhao et al. 2014). This decay channel is denoted as Channel II.

Finally, allowing for finite- $\rho_i k_{0\perp}$  effects in the pump Alfvén wave, we found that the product Alfvén wave is driven by the nonlinear current  $\propto n_S \mathbf{v}_{ipA} + n_A \mathbf{v}_{ipS}$  and the nonlinear inertia  $\propto \mathbf{v}_{ipA} \cdot \nabla_\perp \mathbf{v}_{ipS} \times \hat{\mathbf{z}} + \mathbf{v}_{ipS} \cdot \nabla_\perp \mathbf{v}_{ipA} \times \hat{\mathbf{z}}$ . Here  $n_S$  ( $n_A$ ) and  $\mathbf{v}_{ipS}$  ( $\mathbf{v}_{ipA}$ ) are perturbed ion number density and ion velocity along  $\hat{\mathbf{e}}_p \equiv \hat{\mathbf{e}}_t \times \hat{\mathbf{z}}$  in the slow (Alfvén) wave,  $\rho_i$  is the ion gyroradius, and subscript  $S$  denotes the slow wave. The nonlinear forces driving the slow wave are the nonlinear ion inertial force  $\propto m_i \mathbf{v}_{ipA} \cdot \nabla_\perp \mathbf{v}_{iA}$ , nonlinear ion Lorentz force  $\propto e(\mathbf{v}_{ipA} \times \mathbf{B}_\perp) \cdot \hat{\mathbf{z}}$ , and electron Lorentz force  $\propto -e(\mathbf{v}_{epA} \times \mathbf{B}_\perp) \cdot \hat{\mathbf{z}}$ . In addition to Channels I and II, the finite- $\rho_i k_{0\perp}$  pump Alfvén wave can also decay into the forward Alfvén and backward slow waves (Hasegawa & Chen 1976). This third decay is denoted as Channel III.

Zhao et al. (2015a) considered the nonlinear coupling between the Alfvén and slow waves via the vector-type nonlinear terms proportional to  $n_S \mathbf{v}_{ipA} + n_A \mathbf{v}_{ipS}$ ,  $\mathbf{v}_{ipA} \cdot \nabla_\perp \mathbf{v}_{ipS} \times \hat{\mathbf{z}} + \mathbf{v}_{ipS} \cdot \nabla_\perp \mathbf{v}_{ipA} \times \hat{\mathbf{z}}$ ,  $m_i \mathbf{v}_{ipA} \cdot \nabla_\perp \mathbf{v}_{iA}$ ,  $e(\mathbf{v}_{ipA} \times \mathbf{B}_\perp) \cdot \hat{\mathbf{z}}$ , and  $-e(\mathbf{v}_{epA} \times \mathbf{B}_\perp) \cdot \hat{\mathbf{z}}$  and discovered a three-dimensional (3D) “vector” decay of obliquely propagating MHD Alfvén waves. By comparing this vector decay to the previously known “scalar” decay driven by the scalar nonlinearities  $n_S v_{iA}$ ,  $(\mathbf{v}_{iA} \times \mathbf{B}_\perp) \cdot \hat{\mathbf{z}}$ , and  $(\mathbf{v}_{iA} \cdot \nabla_\perp) v_{iA}$ , Zhao et al. (2015a) concluded that the scalar and vector decays operate in two opposite wavenumber limits: scalar decay operates in the limit  $k_{0\perp} \ll k_{tr}$  and the vector decay operates in the limit  $k_{0\perp} \gg k_{tr}$ , where  $\rho_i k_{tr} \approx \sqrt{\omega / \omega_{ci}}$  is the “turnover” wavenumber,  $\omega$  is the pump wave frequency, and  $\omega_{ci}$  is the ion cyclotron frequency. It has been demonstrated that the vector decay can operate in all three decay channels, generating product waves propagating obliquely to the  $(\mathbf{B}_0, \mathbf{k}_0)$  plane (Zhao et al. 2015a). In this case, the nature

of the decay is essentially 3D, in contrast to the one-dimensional (1D) and two-dimensional (2D) decays studied before (Galeev & Oraevskii 1963; Goldstein 1978), where all wavevectors reside in the  $(\mathbf{B}_0, \mathbf{k}_0)$  plane.

Scalar and vector nonlinearities analyzed separately by Zhao et al. (2014, 2015a) describe the decay in two opposite wavenumber limits but not inbetween. To investigate the nonlinear decay of Alfvén waves in the general case of arbitrary wavelengths, including also an extended range of transition wavenumbers, we now keep both scalar and vector nonlinearities simultaneously. In addition to the decay rate analyzed by Zhao et al. (2015a), here we present a more comprehensive analysis, including also the nonlinear frequency shift. The results are applied to the broadband wavenumber distribution of Alfvén waves in the solar wind.

The organization of the study is as follows. Section 2 presents nonlinear dispersion equations and their solutions describing the nonlinear interaction among Alfvén and slow waves. Section 3 describes the main properties of the nonlinear Alfvénic decay in solar wind conditions. Discussion and summary are included in Sections 4 and 5, respectively.

## 2. Nonlinear Equations and Dispersion Relations

To consider the nonlinear wave–wave interaction among low-frequency waves in a magnetized plasma, we adopt the basic nonlinear two-fluid and Maxwell’s equations:

$$\partial_t \mathbf{v}_\alpha - \frac{q_\alpha}{m_\alpha} (\mathbf{E} + \mathbf{v}_\alpha \times \mathbf{B}_0) + \frac{1}{n_0 m_\alpha} \nabla P_\alpha = \mathbf{NLvel}_\alpha; \quad (1)$$

$$\partial_t n_\alpha + \nabla \cdot (n_0 \mathbf{v}_\alpha) = \mathbf{NLden}_\alpha; \quad (2)$$

$$\nabla \times \mathbf{B} = \mu_0 \mathbf{J}; \quad (3)$$

$$\nabla \times \mathbf{E} = -\partial_t \mathbf{B}, \quad (4)$$

with the nonlinear terms

$$\mathbf{NLvel}_\alpha = -\mathbf{v}_\alpha \cdot \nabla \mathbf{v}_\alpha + \frac{q_\alpha}{m_\alpha} \mathbf{v}_\alpha \times \mathbf{B} + \frac{1}{n_0 m_\alpha} \frac{n_\alpha}{n_0} \nabla P_\alpha; \\ \mathbf{NLden}_\alpha = -\nabla \cdot (n_\alpha \mathbf{v}_\alpha),$$

where  $\mathbf{v}_\alpha$ ,  $n_\alpha$ ,  $\mathbf{E}$ ,  $\mathbf{B}$ , and  $\mathbf{J}$  denote the velocity, number density, electric field, magnetic field, and current density, respectively.  $q_\alpha$ ,  $m_\alpha$ ,  $T_\alpha$ , and  $P_\alpha = T_\alpha (n_0 + n_\alpha)$  denote the particle charge, mass, temperature, and thermal pressure, respectively, for species  $\alpha = i$  for ions and  $\alpha = e$  for electrons. Here,  $n_0$  and  $\mathbf{B}_0$  denote the background number density and magnetic field, respectively. Since we consider low-frequency waves, the displacement current in Ampere’s law is neglected.

Using Equations (1)–(4), Zhao et al. (2014) have derived the general nonlinear equation that describes the nonlinear dynamics of low-frequency Alfvén, slow, and fast mode waves. Here we do not repeat the detailed derivations, the interested reader can refer to Zhao et al. (2014). For the nonlinear interaction between obliquely propagating Alfvén and slow waves in the plasmas with  $m_e/m_i \ll \beta \ll 1$ , the set of nonlinearly coupled equations for Alfvén and slow waves

reads as

$$\begin{aligned}
& [(1 - \rho^2 \partial_\perp^2) \partial_t^2 - V_T^2 \partial_z^2] \partial_z^2 \frac{n_S}{n_0} \\
&= \frac{\mu_0}{B_0} \partial_z^2 \partial_t^2 \mathbf{NLcur}_\perp \cdot \hat{\mathbf{e}}_p - \frac{\mu_0}{B_0 \omega_{ci}} \partial_\perp^2 \partial_t^3 \mathbf{NLcur}_\perp \cdot \hat{\mathbf{e}}_t \\
&+ \frac{\mu_0 e \lambda_e^2}{m_i} \left( \partial_z^2 + \frac{1}{\omega_{ci}^2} \partial_\perp^2 \partial_t^2 \right) \partial_\perp \partial_z \mathbf{NLcur}_\parallel \\
&+ \partial_\perp \partial_z^2 \mathbf{NLden}_t, \tag{5}
\end{aligned}$$

and

$$\begin{aligned}
& [\partial_t^2 - (1 - \rho^2 \partial_\perp^2) V_A^2 \partial_z^2] \partial_t \frac{B_{pA}}{B_0} = \frac{\mu_0 \rho V_T}{B_0} \partial_z \partial_t^2 \mathbf{NLcur}_\perp \cdot \hat{\mathbf{e}}_p \\
&- \frac{\mu_0 V_A^2}{B_0} (1 - \rho^2 \partial_\perp^2) \partial_t \partial_z \mathbf{NLcur}_\perp \cdot \hat{\mathbf{e}}_t \\
&+ \frac{\mu_0 \lambda_e^2}{B_0} \partial_t^2 \partial_\perp \mathbf{NLcur}_\parallel + \rho V_T \partial_\perp \partial_z \mathbf{NLden}_t, \tag{6}
\end{aligned}$$

with nonlinear terms

$$\begin{aligned}
\mathbf{NLcur}_\perp &\equiv \frac{n_0 m_i}{B_0} \left[ \left( \mathbf{NLvel}_{i\perp} + \frac{m_e}{m_i} \mathbf{NLvel}_{e\perp} \right) \times \hat{\mathbf{z}} \right. \\
&\quad \left. + \frac{1}{\omega_{ci}} \partial_t \left( \mathbf{NLvel}_{i\perp} - \frac{m_e^2}{m_i^2} \mathbf{NLvel}_{e\perp} \right) \right] + \frac{n}{n_0} \mathbf{J}_\perp; \\
\mathbf{NLcur}_\parallel &\equiv n_0 e (\mathbf{NLvel}_i - \mathbf{NLvel}_e) \cdot \hat{\mathbf{z}} + \partial_t \left( \frac{n}{n_0} J_\parallel \right); \\
\mathbf{NLden}_t &= -\frac{1}{\omega_{ci}} \partial_t \nabla \cdot \left( \frac{1}{\omega_{ci}} \partial_t \mathbf{NLvel}_{i\perp} + \mathbf{NLvel}_{i\perp} \times \hat{\mathbf{z}} \right) \\
&\quad - \partial_z \mathbf{NLvel}_i \cdot \hat{\mathbf{z}} + \frac{1}{n_0} \partial_t \mathbf{NLden}_i,
\end{aligned}$$

where  $V_T$  is the ion acoustic speed,  $V_A$  is the Alfvén speed, and  $\rho = V_T/\omega_{ci}$ . The three unit axes are defined as  $\hat{\mathbf{e}}_p = \nabla_\perp \times \hat{\mathbf{z}}/|\nabla_\perp|$ ,  $\hat{\mathbf{e}}_t = \nabla_\perp/|\nabla_\perp|$ , and  $\hat{\mathbf{z}} \parallel \mathbf{B}_0$ .

Keeping dominant nonlinear terms, Equations (5)–(6) reduce to

$$\begin{aligned}
& [(1 - \rho^2 \partial_\perp^2) \partial_t^2 - V_T^2 \partial_z^2] \partial_z \frac{n_S}{n_0} \\
&= -\frac{e}{m_i} \partial_z^2 [(\mathbf{v}_{iA} + \mathbf{v}_{iPA}) \times \mathbf{B}_{pA}] \cdot \hat{\mathbf{z}} \\
&+ \frac{e}{m_i} \left( \partial_z^2 + \frac{1}{\omega_{ci}^2} \partial_t^2 \partial_\perp^2 \right) (\mathbf{v}_{ePA} \times \mathbf{B}_{pA}) \cdot \hat{\mathbf{z}} \\
&+ \partial_z^2 (\mathbf{v}_{iA} + \mathbf{v}_{iPA}) \cdot \nabla v_{iZA}; \tag{7}
\end{aligned}$$

$$\begin{aligned}
& [\partial_t^2 - (1 - \rho^2 \partial_\perp^2) V_A^2 \partial_z^2] \partial_\perp \frac{B_{pA}}{B_0} \\
&= -\omega_{ci} (1 - \rho^2 \partial_\perp^2) \partial_z \nabla_\perp \cdot \left( \frac{n_S}{n_0} \mathbf{v}_{iA} \right) \\
&- \omega_{ci} \rho^2 \partial_\perp^2 \partial_z \nabla_\perp \cdot \left( \frac{n_S}{n_0} \mathbf{v}_{iPA} + \frac{n_A}{n_0} \mathbf{v}_{iPS} \right) \\
&+ \partial_z \nabla_\perp \cdot (\mathbf{v}_{iPA} \cdot \nabla \mathbf{v}_{iPS} \times \hat{\mathbf{z}} + \mathbf{v}_{iPS} \cdot \nabla \mathbf{v}_{iPA} \times \hat{\mathbf{z}}). \tag{8}
\end{aligned}$$

Both scalar and vector nonlinearities are kept in Equations (7) and (8), which makes them different from the basic nonlinear equations used by Zhao et al. (2015a), where Equations (1)–(2) contain only scalar nonlinear effects and Equations (3)–(4) only vector ones.

Here we study a three-wave resonant interaction among the pump Alfvén wave ( $\omega_0, \mathbf{k}_0$ ), product Alfvén wave ( $\omega_1, \mathbf{k}_1$ ), and product slow wave ( $\omega_2, \mathbf{k}_2$ ), where the frequency  $\omega_0 = \omega_1 + \omega_2$  and wavenumber  $\mathbf{k}_0 = \mathbf{k}_1 + \mathbf{k}_2$  matching conditions are satisfied. All quantities perturbed by the waves are expressed as  $f = (f_k e^{-i\omega t + i\mathbf{k}\cdot\mathbf{r}} + f_k^* e^{i\omega^* t - i\mathbf{k}^*\cdot\mathbf{r}})/2$ . We also assume applicability of the linear wave responses for the perturbed quantities entering the nonlinear terms in Equations (7) and (8). These linear responses for Alfvén and slow waves read as

$$\begin{aligned}
(\mathbf{v}_{iA})_k &= i \frac{s V_A^2 k_z (B_{pA})_k}{\omega_{ci} B_0} \hat{\mathbf{e}}_t; \\
(\mathbf{v}_{iA})_k &= i \frac{V_T \rho k_\perp (B_{pA})_k}{K^2 B_0} \hat{\mathbf{z}}; \\
(\mathbf{v}_{iPA})_k &= -\frac{s V_A (B_{pA})_k}{K B_0} \hat{\mathbf{e}}_p; \\
(\mathbf{v}_{ePA})_k &= -s V_A K \frac{(B_{pA})_k}{B_0} \hat{\mathbf{e}}_p; \\
(n_A)_k &= i \frac{s n_0 V_A k_\perp (B_{pA})_k}{\omega_{ci} K B_0}; \\
(\mathbf{v}_{iPS})_k &= -i V_T \rho k_\perp \frac{(n_S)_k}{n_0} \hat{\mathbf{e}}_p,
\end{aligned}$$

where  $K \equiv \sqrt{1 + \rho^2 k_\perp^2}$ , and  $s$  denotes the wave propagation direction,  $s = 1$  along  $\mathbf{B}_0$  and  $s = -1$  against  $\mathbf{B}_0$ . With these responses, from nonlinear Equations (7) and (8), we obtain the nonlinear dispersion equations

$$(\omega_1^2 - \Omega_1^2) \frac{B_1}{B_0} = C_1 \frac{B_{A0}}{B_0} \frac{n_2^*}{n_0}; \tag{9}$$

$$(\omega_2^2 - \Omega_2^2) \frac{n_2}{n_0} = C_2 \frac{B_{A0}}{B_0} \frac{B_1^*}{B_0}, \tag{10}$$

where

$$\begin{aligned}
\Omega_1 &= V_A k_{1z} K_1; \quad \Omega_2 = \frac{V_T k_{2z}}{K_2}; \\
C_1 &= -\frac{V_A \omega_{ci}}{2} s_1 k_{1z} \left[ \frac{V_A k_{0z}}{\omega_{ci}} K_1^2 (\hat{\mathbf{e}}_{1t} \cdot \hat{\mathbf{e}}_{0t}) \right. \\
&\quad \left. - i \frac{K_0^2 K_1^2 - K_2^2}{K_0} (\hat{\mathbf{e}}_{1t} \times \hat{\mathbf{e}}_{0t}) \cdot \hat{\mathbf{z}} \right]; \\
C_2 &= -\frac{V_A \omega_{ci}}{2} \frac{s_2 k_{2z}}{K_2^2} \left[ \frac{V_A}{\omega_{ci}} \left( \frac{s_1 k_{1z}}{K_0^2} - \frac{k_{0z}}{K_1^2} \right) (\hat{\mathbf{e}}_{1t} \cdot \hat{\mathbf{e}}_{0t}) \right. \\
&\quad \left. - i \frac{K_0^2 K_1^2 - K_2^2}{K_0^2 K_1^2 K_2^2} (s_1 K_1 - K_0) (\hat{\mathbf{e}}_{1t} \times \hat{\mathbf{e}}_{0t}) \cdot \hat{\mathbf{z}} \right].
\end{aligned}$$

The subscripts  $A$  and  $S$  for product Alfvén and slow waves are replaced here by their numbers 1 and 2, such that  $\Omega_1$  and  $\Omega_2$  are their linear dispersions and,  $C_1$  and  $C_2$  are their nonlinear coupling coefficients, respectively. The nonlinear

terms proportional to  $\hat{e}_{1t} \cdot \hat{e}_{0t}$  and  $\hat{e}_{1t} \times \hat{e}_{0t}$  represent scalar and vector nonlinear couplings (Voitenko & Goossens 2005; Zhao et al. 2015a).

The nonlinear coupling terms on the right-hand sides of Equations (9) and (10) produce a nonlinear frequency shift  $\Delta\omega$ , modifying the linear Alfvén and slow mode dispersions:

$$\begin{aligned}\omega_1 &= \Omega_1 - \Delta\omega + i\gamma; \\ \omega_2 &= \Omega_2 + \Delta\omega + i\gamma,\end{aligned}\quad (11)$$

where  $\gamma$  is the nonlinear growth rate. In the derivation of  $\omega_2$ , the resonant condition  $\Omega_0 = \Omega_1 + \Omega_2$  is used, and the pump wave frequency is unaffected in the nonlinear coupling at the initial stage of the decay. In passing, we note that Equation (11) corrects the misprint signs in Equations (A4) and (A5) by Zhao et al. (2015a).

Equations (9) and (10) describe the nonlinear coupling among nondissipative waves. Since the kinetic-scale Alfvén and slow waves undergo Landau damping, we incorporate it into the nonlinear model as (Nishikawa 1968; Zhao et al. 2015a)

$$(\omega_1^2 - \Omega_1^2 - i2\omega_1\gamma_{L1}) \frac{B_{A1}}{B_0} = C_1 \frac{B_{A0}}{B_0} \frac{n_2^*}{n_0}; \quad (12)$$

$$(\omega_2^2 - \Omega_2^2 - i2\omega_2\gamma_{L2}) \frac{n_2}{n_0} = C_2 \frac{B_{A0}}{B_0} \frac{B_{A1}^*}{B_0}. \quad (13)$$

Here

$$\begin{aligned}\frac{\gamma_{L1}}{\Omega_1} &= -\sqrt{\frac{\pi}{8}} \frac{\mu_{1i}^2}{K} \frac{T_e}{T_i} \frac{V_A}{V_{Ti}} \left[ \frac{T_e}{T_i} \Lambda_0 \exp\left(-\frac{V_A^2 K_1^2}{2V_{Ti}^2}\right) \right. \\ &\quad \left. + \frac{V_{Ti}}{V_{Te}} \exp\left(-\frac{V_A^2 K_1^2}{2V_{Ti}^2} \frac{V_{Ti}^2}{V_{Te}^2}\right) \right];\end{aligned}\quad (14)$$

$$\begin{aligned}\frac{\gamma_{L2}}{\Omega_2} &= 0.14 - 0.61 \sqrt{\left(1 + \frac{T_i}{T_e}\right) \frac{0.42 + 0.58\mu_{2i}^2}{0.42 + 0.038\mu_{2i}^2} - 1} \\ &\quad + 0.05 \left[ \left(1 + \frac{T_i}{T_e}\right) \frac{0.42 + 0.58\mu_{2i}^2}{0.42 + 0.038\mu_{2i}^2} - 1 \right],\end{aligned}\quad (15)$$

represent the Landau damping of Alfvén and slow waves, respectively (Zhao et al. 2014),  $\Lambda_0 = I_0(\mu_i^2) \exp(-\mu_i^2)$ ,  $I_0(\mu_i^2)$  is the zero-order modified Bessel function of the first kind, and  $\mu_{1,2i} \equiv \rho_i k_{1,2\perp}$ .

Equations (11)–(13) yield the general nonlinear equation

$$\begin{aligned}[(\Delta\omega + i\gamma)^2 - 2(\Omega_1 + i\gamma_{L1})(\Delta\omega + i\gamma) + i2\Omega_1\gamma_{L1}] \\ \times [(\Delta\omega + i\gamma)^2 + 2(\Omega_2 - i\gamma_{L2})(\Delta\omega + i\gamma) - i2\Omega_2\gamma_{L2}] \\ = C_1^* C_2 \left| \frac{B_{A0}}{B_0} \right|^2.\end{aligned}\quad (16)$$

Using this equation, we are going to explore three channels for the nonlinear Alfvénic decay in different wavenumber ranges. In the case of nondissipative waves ( $\gamma_{L1} = \gamma_{L2} = 0$ ) at MHD

scales ( $K_0 = K_1 = K_2 = 1$ ) Equation (16) reduces to

$$\begin{aligned}[(\Delta\omega + i\gamma) - 2\Omega_1][(\Delta\omega + i\gamma) + 2\Omega_2](\Delta\omega + i\gamma)^2 \\ = -\frac{s_1 V_A^4 k_{0z} k_{1z} k_{2z}^2}{4} (\hat{e}_{1t} \cdot \hat{e}_{0t})^2 \left| \frac{B_{A0}}{B_0} \right|^2.\end{aligned}\quad (17)$$

In the limit  $|\Delta\omega + i\gamma| \ll \Omega_2$  and  $k_{2z} \simeq 2k_{0z}$ , (17) gives the nonlinear growth rate

$$\gamma_{\max} = \frac{\omega_0}{2\sqrt{2}} \sqrt{\frac{V_A}{V_T}} \left| \frac{B_{A0}}{B_0} \right| \quad (18)$$

consistent with the nonlinear growth rate found by Galeev & Oraevskii (1963).

The decay instability can also be driven by the four-wave coupling among MHD scale Alfvén and slow waves (Derby 1978; Goldstein 1978). The general dispersion equation was derived by Goldstein (1978)

$$\begin{aligned}(\omega^2 - \beta k^2)(\omega - k)[(\omega + k)^2 - 4] \\ = \frac{1}{2} \eta k^2 (\omega^3 + \omega^2 k - 3\omega k + k),\end{aligned}$$

where  $\eta \equiv (B_{A0}/B_0)^2$ , and  $\omega$  and  $k$  are normalized by  $\omega_0$  and  $k_0$ . Note that the coefficient “1/2” is lost in the dispersion relation by Derby (1978) who treated perturbation as  $\delta f = \delta f(\omega, k) \exp(-i\omega t + kz)$ , whereas Goldstein (1978) used  $\delta f = \frac{1}{2} [\delta f(\omega, k) \exp(-i\omega t + kz) + \delta f^*(\omega, k) \exp(i\omega^* t + kz)]$  adopted also in our derivation. By analyzing the unstable mode of the general dispersion equation by Derby (1978), Jayanti & Hollweg (1993) found the maximal growth rate of the Alfvén decay to be  $\frac{\omega_0}{2} \sqrt{\frac{V_A}{V_T} \eta}$ . Hence, the expression (18) can be recovered from the Goldstein’s dispersion equation.

### 3. Decay of Alfvén Waves in the Solar Wind

Alfvén waves permeating the interplanetary space have a broadband wavenumber spectrum extending from MHD to ion kinetic scales (e.g., Leamon et al. 1998; Bale et al. 2005; Roberts et al. 2015). According to observational and theoretical results, the amplitude and frequency of Alfvén waves can be expressed as

$$\frac{B_{\perp}}{B_0} = (1 + \rho^2 k_{\perp}^2)^{-1/6} (k_{\perp}/k_{\perp, \text{in}})^{-1/3} \frac{B_{\text{in}}}{B_0}, \quad (19)$$

and

$$\frac{\omega_0}{\omega_{ci}} = (1 + \rho^2 k_{\perp}^2)^{-1/6} (k_{\perp}/k_{\perp, \text{in}})^{2/3} \frac{\omega_{\text{in}}}{\omega_{ci}}, \quad (20)$$

where  $k_{\text{in}}$ ,  $B_{\text{in}}$ , and  $\omega_{\text{in}}$  are the perpendicular wavenumber, magnetic field, and frequency of Alfvén waves at the largest injection scale. We will assume  $T_e/T_i = 1$  and, except where other values are indicated,  $\rho_i k_{\text{in}} = 10^{-4}$ ,  $B_{\text{in}}/B_0 = 0.3$ , and  $\omega_{\text{in}}/\omega_{ci} = 10^{-4}$  for the waves at the injection scale, which is typical for the inner solar wind. The same Alfvén wave distribution has been used by Zhao et al. (2015a) to estimate their decay rate in some wavelength limits in the solar wind conditions. In the present study, we explore the Alfvén decay and its evolution from largest MHD to smallest kinetic scales, including an extended wavenumber range where the scalar and vector nonlinear interactions operate simultaneously.

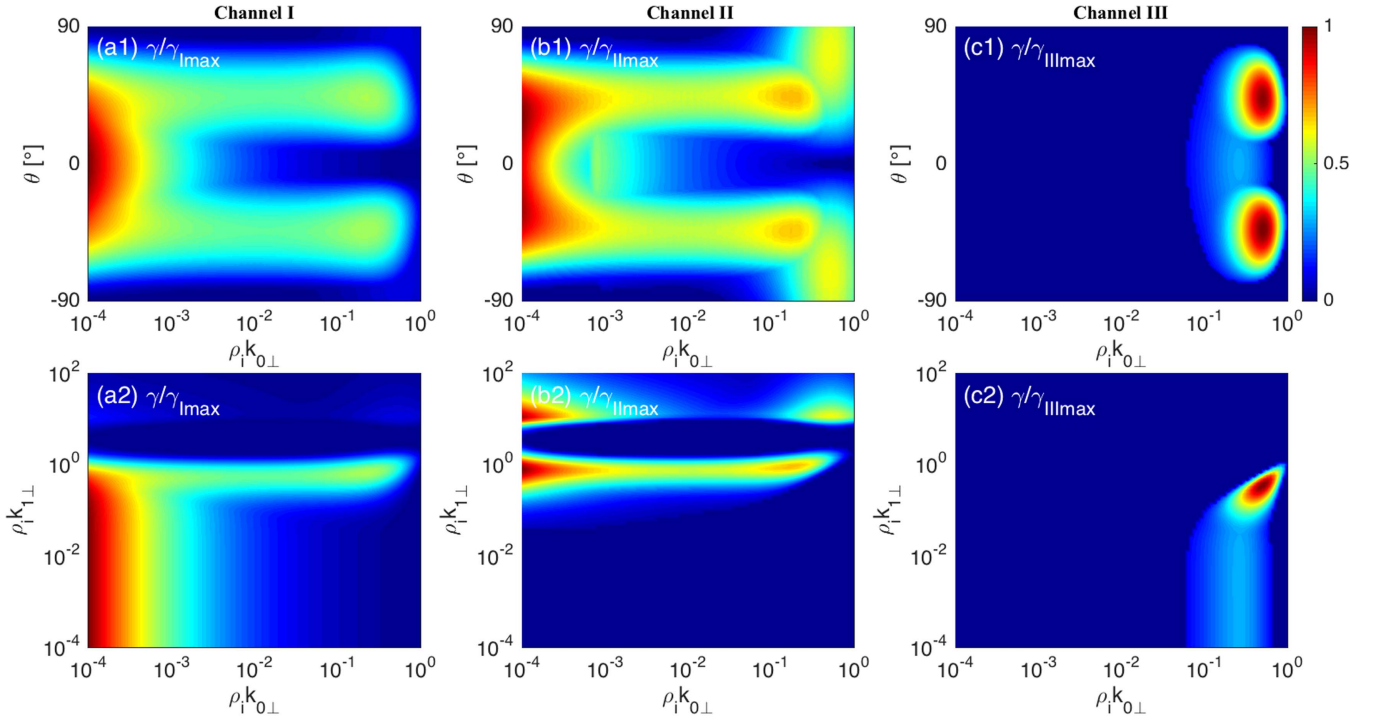


**Figure 1.** Top panels present the nonlinear growth rate  $\gamma/\gamma_{\max}$  as a function of  $\rho_i k_{0\perp}$  and angle  $\theta$  between perpendicular wavevectors of two Alfvén waves: Channel I (a1), Channel II (b1), and Channel III (c1). Bottom panels present  $\gamma/\gamma_{\max}$  as a function of  $\rho_i k_{0\perp}$  and  $\rho_i k_{1\perp}$ : Channel I (a2), Channel II (b2), and Channel III (c2).  $\gamma_{\text{I max}}/\Omega_0 = 0.23$ ,  $\gamma_{\text{II max}}/\Omega_0 = 0.03$ , and  $\gamma_{\text{III max}}/\Omega_0 = 0.01$  correspond to the maximal growth rates in Channels I, II, and III.

Using Equation (16) with amplitudes (19) and frequencies (20), in panels (a1)–(c1) of Figure 1, we show the 2D distribution of the normalized growth rate  $\gamma/\gamma_{\max}$  as a function of the perpendicular wavenumber  $\rho_i k_{0\perp}$  and angle  $\theta$  between perpendicular wavevectors of two Alfvén waves. The decay is of scalar type when  $\gamma/\gamma_{\max}$  is peaked at  $\theta = 0$ , and of vector type when the maximum(s) is at  $\theta \neq 0$ . In Channel I, at the smallest wavenumbers  $\rho_i k_{0\perp}$ , the maximal growth rate is attained at  $\theta \approx 0^\circ$ . With increasing  $\rho_i k_{0\perp}$ , the single maximum of  $\gamma/\gamma_{\text{I max}}$  splits into two at  $\theta \sim \pm 45^\circ$ . The transition is smooth and occupies about one decade from  $\rho_i k_{0\perp} \gtrsim 10^{-4}$  to  $\rho_i k_{0\perp} \gtrsim 10^{-3}$ , with the “mean” transition wavenumber  $\rho_i k_{\text{tr}} \sim 5 \times 10^{-4}$ . It is thus clear that the transition occurs at significantly smaller wavenumbers than the wavenumber  $\rho_i k_{\text{tr}} \sim \sqrt{\omega/\omega_{ci}} \sim 10^{-2}$  predicted theoretically by Zhao et al. (2015a). In Channel II, the transition occurs even earlier, at smaller wavenumbers around  $\rho_i k_{\text{tr}} \sim 10^{-4}$ , where the maximum of the growth rate splits into two at  $\theta \sim \pm 45^\circ$ . When passing through the ion kinetic scales  $\rho_i k_{0\perp} \sim 1$ , these two maxima move farther apart from each other up to  $\theta \sim \pm 90^\circ$ , which is governed by the combined action of scalar and vector nonlinear effects. In Channel III the decay is limited to the ion kinetic scales  $\rho_i k_{0\perp} \sim 0.5$  and has two maxima at azimuthal angles  $\theta \sim \pm 45^\circ$ .

The behavior of the growth rate described above indicates that, except for the pump Alfvén waves of largest scales  $\rho_i k_{0\perp} \sim 10^{-4}$ , the product waves generated by the decay propagate out of the  $(\mathbf{k}_{0\perp}, \mathbf{B}_0)$  plane. All decay channels are therefore essentially 3D; only Channel I at the largest scales is 2D. In accordance to Zhao et al. (2015a), the large-scale decay with maximum at  $\theta \sim 0^\circ$  is dominated by the scalar-type nonlinear interactions, whereas other decays with peaks at  $\theta \neq 0^\circ$  are contributed or dominated by the vector-type interactions. In addition, we also observe kinetic-scale

obliquely propagating product waves generated by the joint action of scalar- and vector-type nonlinear interactions.

Panels (a2)–(c2) in Figure 1, showing the nonlinear growth rate  $\gamma/\gamma_{\max}$  as a function of  $\rho_i k_{0\perp}$  and  $\rho_i k_{1\perp}$ , are particularly useful to distinguish local and nonlocal decay processes. In Channel I, the large-scale Alfvén waves with  $10^{-4} < \rho_i k_{0\perp} < 10^{-3}$  excite broadband Alfvén waves in the wide range from MHD to kinetic scales,  $10^{-4} < \rho_i k_{1\perp} < 1$ . The picture changes at  $\rho_i k_{0\perp} \gtrsim 10^{-3}$  where the product waves are concentrated in the relatively narrow kinetic-scale range at  $\rho_i k_{0\perp} \lesssim 1$ . In Channel II, the pump Alfvén waves produce kinetic-scale Alfvén waves peaked at  $\rho_i k_{1\perp} \sim 1$  and  $\rho_i k_{1\perp} \sim 10$ . The heavy depression of the growth rate observed between these two peaks is contributed mainly to the strong Landau damping therein (Zhao et al. 2014). In Channel III, only the pump Alfvén waves with  $\rho_i k_{0\perp} \sim 0.5$  can decay, generating the product Alfvén wave with similar wavenumbers  $k_{1\perp} \sim k_{0\perp}$ . The conclusion is as follows: Alfvén waves with  $\rho_i k_{0\perp} \geq 10^{-3}$  from the solar wind spectrum tend to decay nonlocally, generating distant kinetic-scale wavenumbers  $\rho_i k_{1\perp} \sim 1$ . At larger scales the decay tends to be local, generating similar wavenumbers.

Figure 2 presents the normalized nonlinear frequency shifts of the product waves  $\Delta\omega/\Omega_1$  and  $\Delta\omega/\Omega_2$  as functions of  $\theta$  and  $\rho_i k_{0\perp}$ . Note that different color bars are used to show  $\Delta\omega/\Omega_1$  and  $\Delta\omega/\Omega_2$  in Figure 2, as well as  $\gamma/\Omega_0$ ,  $\Delta\omega/\Omega_1$ , and  $\Delta\omega/\Omega_2$  in the following figures. In the wavenumber space, both  $\Delta\omega/\Omega_1$  and  $\Delta\omega/\Omega_2$  behave similarly to  $\gamma$ , except for Channel II at  $\rho_i k_{1\perp} > 0.4$  and for Channel III at nearly  $\rho_i k_{1\perp} \sim 0.1$ . Furthermore, panels (a3)–(c3) display the maximal nonlinear growth rate  $\gamma_{\max}/\Omega_0$  and the corresponding nonlinear frequency shifts  $\Delta\omega/\Omega_1$  and  $\Delta\omega/\Omega_2$ . It is seen that the decay rates in Channels I, II, and III are arranged as  $\gamma_{\text{max}}^{\text{I}}/\Omega_0 >$

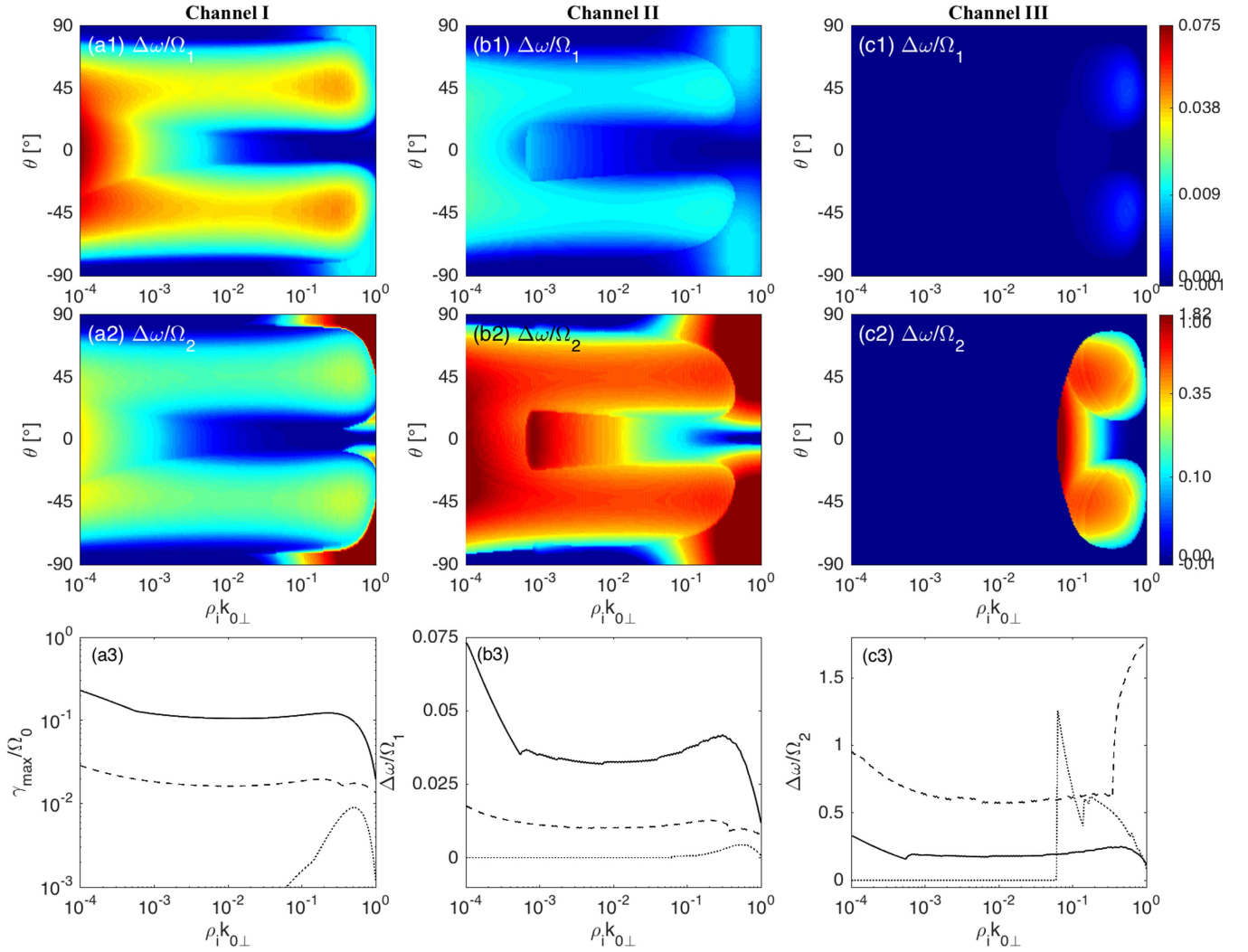


**Figure 2.** Nonlinear frequency shifts  $\Delta\omega/\Omega_1$  (top panels) and  $\Delta\omega/\Omega_2$  (middle panels) as functions of  $\rho_i k_{0\perp}$  and  $\theta$ : Channel I (a1) and (a2); Channel II (b1) and (b2); and Channel III (c1) and (c2). Bottom panels present the maximal growth rate  $\gamma_{\max}/\Omega_0$  and the nonlinear frequency shifts  $\Delta\omega/\Omega_1$  and  $\Delta\omega/\Omega_2$  in Channel I (solid line), Channel II (dashed line), and Channel III (dotted line).

$\gamma_{\max}^{\text{II}}/\Omega_0 > \gamma_{\max}^{\text{III}}/\Omega_0$ . Since the nonlinear frequency shift  $\Delta\omega/\Omega_1$  is always much smaller than 0.1, the product Alfvén waves can be approximated as normal modes. In the strongest Channel I,  $\Delta\omega/\Omega_2$  is slightly smaller than 0.3, and in the other two channels it is slightly larger than 0.5. Such large values of  $\Delta\omega/\Omega_2$  mean that the product slow waves deviate considerably from the normal modes. Note that only the data corresponding to  $\gamma/\Omega_0 > 10^{-3}$  are retained.

In order to study the dependence of  $\gamma/\Omega_0$ ,  $\Delta\omega/\Omega_1$ , and  $\Delta\omega/\Omega_2$  on the wave and plasma parameters, we change the initial wave amplitude to  $B_{\text{in}}/B_0 = 0.5$  in Figure 3, the initial wave frequency to  $\omega_{\text{ini}}/\omega_{\text{ci}} = 0.5 \times 10^{-4}$  in Figure 4, the plasma  $\beta_i$  to  $\beta_i = 0.1$  in Figure 5, and the temperature ratio to  $T_e/T_i = 3$  in Figure 6, keeping other parameters the same as in Figures 1 and 2.

Comparison of Figures 2 and 3 shows that  $\gamma/\Omega_0$  is larger for larger wave amplitude ( $\gamma_{\max}^{\text{I}}/\Omega_0 \approx 0.36$  for  $B_{\text{in}}/B_0 = 0.5$  and  $\gamma_{\max}^{\text{I}}/\Omega_0 \approx 0.23$  for  $B_{\text{in}}/B_0 = 0.3$ ), but does not follow the usual scaling  $\gamma/\Omega_0 \sim (B_{\perp}/B_0)$ . For  $B_{\text{in}}/B_0 = 0.5$ ,  $\Delta\omega/\Omega_1 < 0.13$  and  $\Delta\omega/\Omega_2 \sim 0.4$  in Channel I, and  $\Delta\omega/\Omega_2 > 1$  in the other two channels, which means that the product Alfvén

waves are still the normal modes, whereas the product slow waves deviate further from the normal modes.

It is interesting to observe in Figure 4 that the maximum growth rates  $\gamma_{\max}^{\text{I}}/\Omega_0 \approx 0.26$  and  $\gamma_{\max}^{\text{II}}/\Omega_0 \approx 0.053$  remain nearly constant, while  $\rho_i k_{0\perp}$  varies in a wide range from  $10^{-4}$  to 0.5. On the contrary, comparing Figure 4 to Figure 2, we see that  $\Delta\omega/\Omega_1$  and  $\Delta\omega/\Omega_2$  become larger for smaller  $\omega_{\text{ini}}/\omega_{\text{ci}}$ , resulting in larger departures from the normal modes.

In Figure 5, where  $\beta_i$  is higher, the nonlinear growth rate  $\gamma/\Omega_0$  is depressed as compared to Figure 2, where  $\beta_i$  is lower. The nonlinear frequency shifts  $\Delta\omega/\Omega_1$  and  $\Delta\omega/\Omega_2$  are also highly reduced in the higher- $\beta_i$  cases, which implies that the product waves are close to the normal modes.

With larger  $T_e/T_i$ , as in Figures 6, the growth rate  $\gamma_{\max}/\Omega_0$  is normally larger (smaller) in Channel I (Channel II). Also,  $\gamma_{\max}/\Omega_0$  becomes larger at smaller  $\rho_i k_{0\perp}$ . In the wavenumber range  $\rho_i k_{0\perp} \lesssim 0.5$ , both  $\Delta\omega/\Omega_1$  and  $\Delta\omega/\Omega_2$  are smaller when  $T_e/T_i$  is larger. It is thus easier to find product Alfvén and slow waves as normal modes at larger  $T_e/T_i$ .

The general trend observed in Figures 1, 3, and 4 for all three channels (except for Channel I at the lowest wavenumbers  $\rho_i k_{0\perp} \sim 10^{-4}$ ) is the 3D and nonlocal character of the Alfvén-wave decay in the solar wind. The nonlocality is reflected in

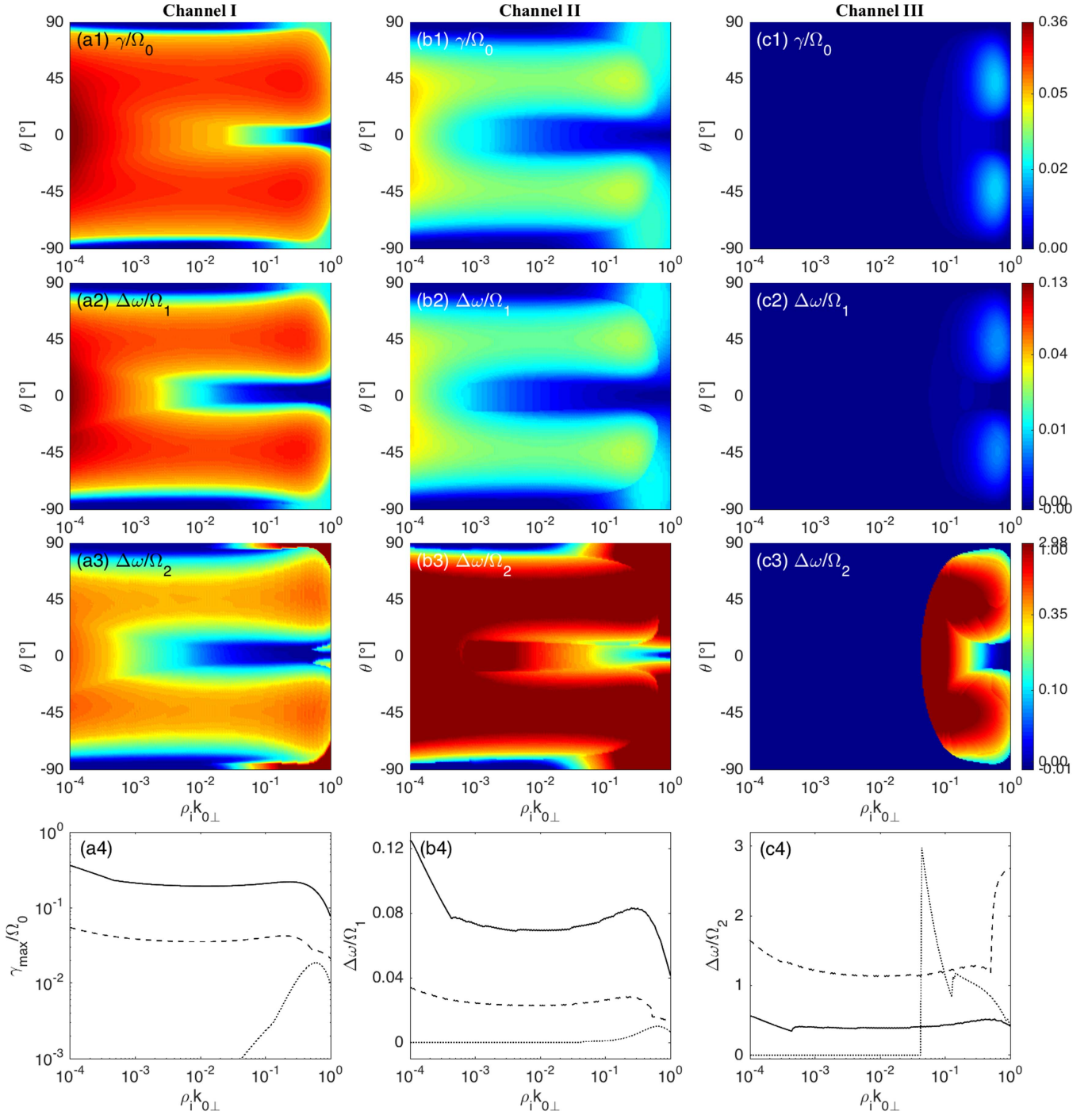


**Figure 3.** Nonlinear growth rate  $\gamma/\Omega_0$  (top panels), and the nonlinear frequency shifts  $\Delta\omega/\Omega_1$  (second panels) and  $\Delta\omega/\Omega_2$  (third panels) as functions of  $\rho_i k_{0\perp}$  and  $\theta$ : Channel I (a1), (a2), and (a3); Channel II (b1), (b2), and (b3); and Channel III (c1), (c2), and (c3). Bottom panels present the maximal growth rate  $\gamma_{\max}/\Omega_0$  as well as nonlinear frequency shifts  $\Delta\omega/\Omega_1$  and  $\Delta\omega/\Omega_2$ , where the solid, dashed, and dotted lines represent Channels I, II, and III, respectively. Here the amplitude of the pump wave at injection is  $B_{\text{in}}/B_0 = 0.5$ .

both the wavenumber ( $k_{1\perp}$ ) distribution and the azimuthal angular ( $\theta$ ) distribution of the product waves. As a consequence, the Alfvén wave decay can generate a nonlocal spectral transport of the wave energy over several decades from the MHD scales directly to the ion kinetic scales.

#### 4. Discussion

When Alfvén waves propagate outward from the Sun, their amplitudes increase with the radial distance in the inner solar

wind. Observations of radio scintillations have demonstrated that the transverse velocity fluctuations are  $\sim 50\text{--}300\text{ km s}^{-1}$  at radial distances  $r \sim 20\text{--}60R_S$  in the fast solar wind (Canals et al. 2002). With the Alfvén speed  $\sim 600\text{ km s}^{-1}$ , such velocities give the relative magnetic amplitudes of Alfvén waves  $\sim 0.1\text{--}0.5$ . Several simulations have reproduced similar amplitudes of Alfvén waves in the inner solar wind at  $r \sim 20\text{--}60 R_S$  (Cranmer & van Ballegoijen 2005; Suzuki & Inutsuka 2005; Verdini & Velli 2007). These high-amplitude Alfvén waves can undergo nonlinear decay, which has been

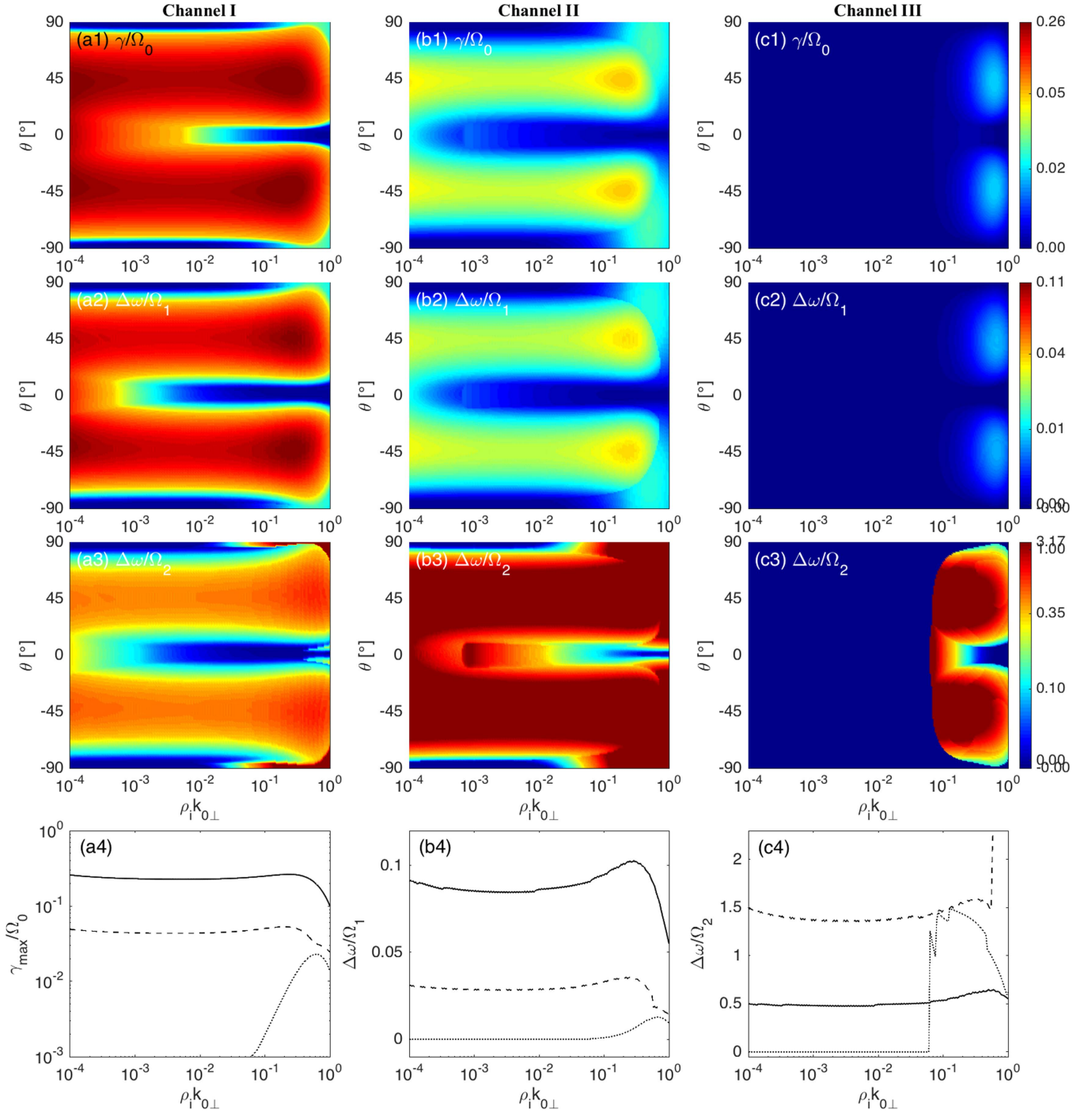


**Figure 4.** Nonlinear growth rate  $\gamma/\Omega_0$  (top panels), and the nonlinear frequency shifts  $\Delta\omega/\Omega_1$  (second panels) and  $\Delta\omega/\Omega_2$  (third panels) as functions of  $\rho_i k_{0\perp}$  and  $\theta$ : Channel I (a1), (a2), and (a3); Channel II (b1), (b2), and (b3); and Channel III (c1), (c2), and (c3). Bottom panels present the maximal growth rate  $\gamma_{\max}/\Omega_0$  as well as nonlinear frequency shifts  $\Delta\omega/\Omega_1$  and  $\Delta\omega/\Omega_2$ , where the solid, dashed, and dotted lines represent Channels I, II, and III, respectively. Here the frequency of the pump wave at injection is  $\omega_{in}/\omega_0 = 0.5 \times 10^{-4}$ .

demonstrated by many MHD simulations (e.g., Suzuki & Inutsuka 2005, 2006; Matsumoto & Suzuki 2012; Tenerani & Velli 2013). In the case of relative amplitudes  $\sim 0.5$ , the maximum growth rate may reach  $\sim 0.3\omega$ , as one can see in Figure 3.

Through the decay, original Alfvén waves dissipate nonlinearly, transferring a fraction of their energy to the slow waves. In turn, these slow waves can develop shocks heating plasma in the solar corona and solar wind (Del Zanna et al. 2001; Suzuki & Inutsuka 2005, 2006). Also, the slow wave can

heat ions through the Landau damping (Narita & Marsch 2015), or can trap ions in electrostatic potential wells and accelerate them (e.g., Terasawa et al. 1986; Maneva et al. 2015). On the other hand, a steepening of the Alfvén wave can arise due to the local density inhomogeneity induced by the slow wave (Cohen & Kulsrud 1974; Shoda & Yokoyama 2016). Moreover, the Alfvénic turbulence may develop through nonlinear interactions between the forward pump waves and counter-propagating product Alfvén waves (Matsumoto & Suzuki 2012). Nonlinear decay, wave steepening, and

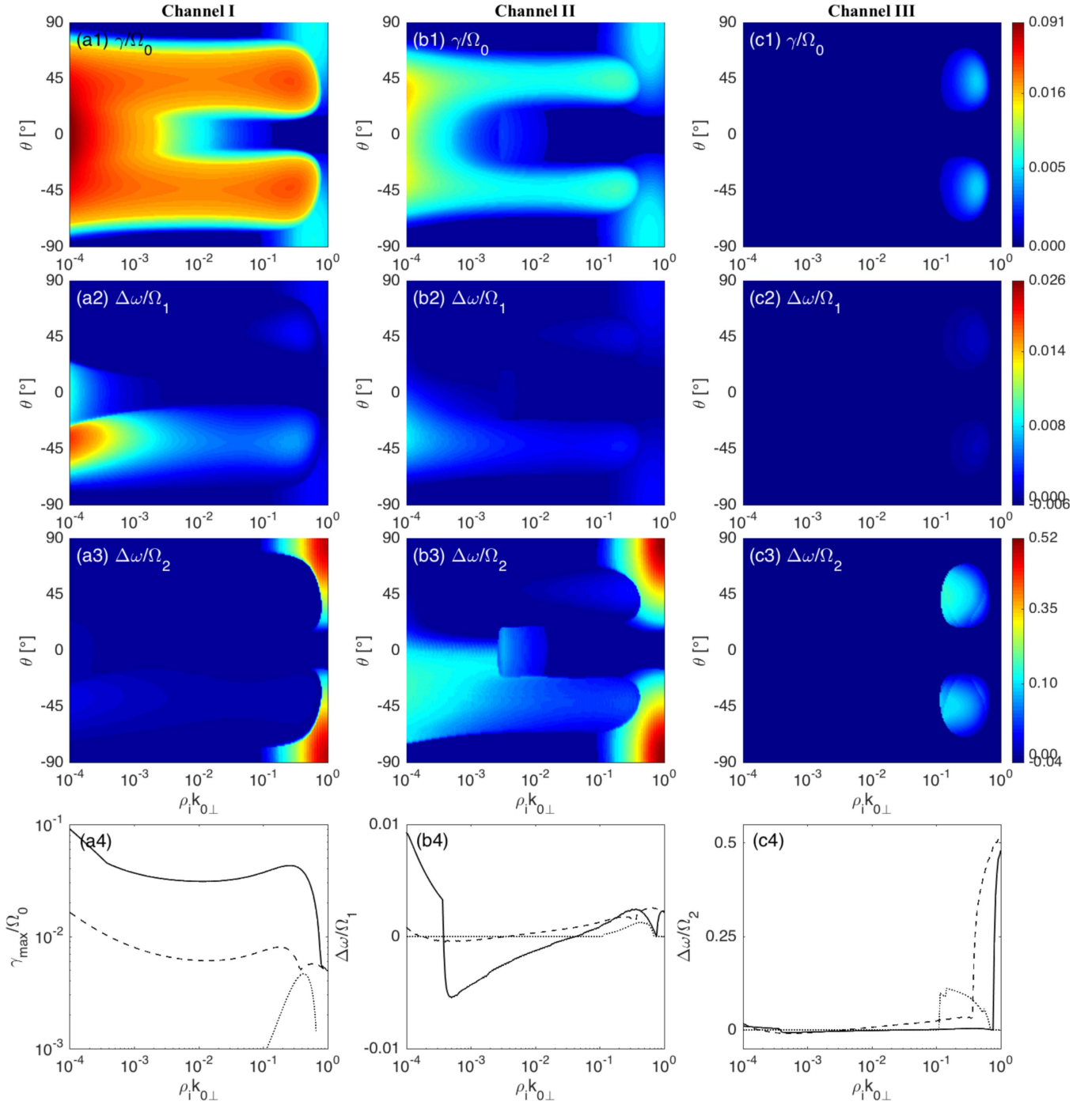


**Figure 5.** Nonlinear growth rate  $\gamma/\Omega_0$  (top panels), and the nonlinear frequency shifts  $\Delta\omega/\Omega_1$  (second panels) and  $\Delta\omega/\Omega_2$  (third panels) as functions of  $\rho_i k_{0\perp}$  and  $\theta$ : Channel I (a1), (a2), and (a3); Channel II (b1), (b2), and (b3); and Channel III (c1), (c2), and (c3). Bottom panels present the maximal growth rate  $\gamma_{\max}/\Omega_0$  as well as nonlinear frequency shifts  $\Delta\omega/\Omega_1$  and  $\Delta\omega/\Omega_2$ , where the solid, dashed, and dotted lines represent Channel I, II, and III, respectively. Here  $\beta_i = 0.1$ .

turbulence are all processes that can contribute to the dissipation of original Alfvén waves.

Previous works were mainly focused on the 1D or 2D decay of the Alfvén wave in the framework of a one-fluid MHD model, as well as on 1D or 2D hybrid simulations (e.g., Del Zanna et al. 2001; Suzuki & Inutsuka 2005; Nariyuki et al. 2014; Maneva et al. 2015). However, the one-fluid MHD model cannot capture all decay channels, in particular, channels involving kinetic effects. The kinetic effects affect the decay even when wavelengths are much larger than the ion gyroscale. As a result, the MHD-scale Alfvén waves can strongly couple

with kinetic-scale Alfvén waves (Zhao et al. 2014). The scalar-type nonlinear forces, that come from both the MHD and kinetic effects, drive broadband Alfvén waves distributed from MHD to ion scales. The vector-type nonlinear forces, which are mainly contributed by the kinetic effects, generate Alfvén waves close to the ion gyroscale. Moreover, for pump wavelengths  $\leq 10^4 \rho_i$ , the 3D vector-type nonlinear forces dominate the Alfvén wave decay (see Figure 1) and cannot be captured by the one-fluid MHD model.

Alfvén wave decay may be responsible for many phenomena observed in the solar wind, like decreasing cross-helicity with

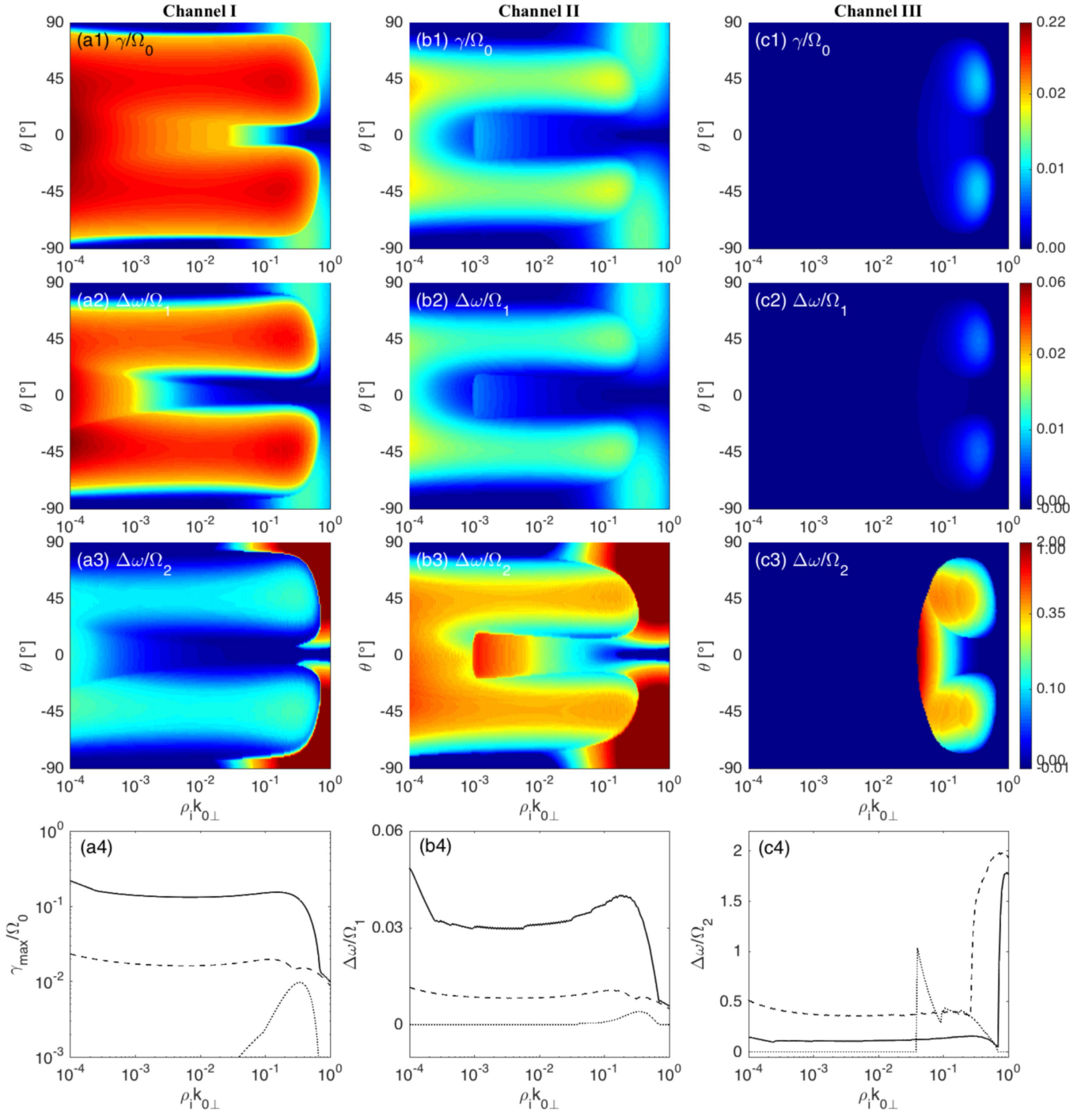


**Figure 6.** Nonlinear growth rate  $\gamma/\Omega_0$  (top panels), and the nonlinear frequency shifts  $\Delta\omega/\Omega_1$  (second panels) and  $\Delta\omega/\Omega_2$  (third panels) as functions of  $\rho_i k_{0\perp}$  and  $\theta$ : Channel I (a1), (a2), and (a3); Channel II (b1), (b2), and (b3); and Channel III (c1), (c2), and (c3). Bottom panels present the maximal growth rate  $\gamma_{\max}/\Omega_0$  as well as nonlinear frequency shifts  $\Delta\omega/\Omega_1$  and  $\Delta\omega/\Omega_2$ , where the solid, dashed, and dotted lines represent Channels I, II, and III, respectively. Here  $T_e/T_i = 3$ .

radial distance (Bavassano et al. 2000), compressible waves (Miyamoto et al. 2014; Shi et al. 2015; Roberts et al. 2017), and inward propagating Alfvén waves in the fast solar wind (He et al. 2015a; Li et al. 2016a; Yang et al. 2016). However, the decay instability itself is not easy to observe directly. The most difficult is the mode identification. First, it is difficult to distinguish the forward/backward Alfvén waves. Second, the slow waves can deviate strongly from the normal modes, in which case their identification based on the linear wave response is impossible. In most cases, the pump Alfvén wave

excites the normal Alfvén eigenmodes and the nonlinear sound-like fluctuations (e.g., Goldstein 1978; Araneda et al. 2007). Only with low wave amplitudes and/or large  $\beta_i$  do the sound-like fluctuations approach the normal wave modes.

In Channel I, the product Alfvén waves propagate against the pump Alfvén waves, which complicates the task of maintaining their correlation time long enough for the nonlinear wave–wave interaction to accomplish the decay. In Figures 1–6, we analyze merely the nonlinear decay with  $10^{-3} < \gamma/\omega_0 < 1$  and  $\omega_{1,2}/\omega_0 > 10^{-4}$ . To achieve the decay in the cases of weaker

growth rates  $\gamma/\omega_0 < 10^{-3}$ , even longer correlation times are needed, which can hardly be satisfied in the turbulent solar wind environment.

It should also be emphasized that, although we took into account the dominant nonlinear forces, there are also some minor forces neglected in our present analysis. For example, the nonlinear electron Lorentz force  $-e(\mathbf{v}_{epA} \times \mathbf{B}_\perp) \cdot \hat{\mathbf{z}}$  in the nonlinear equation of the slow wave and several other minor forces may affect the decay in special circumstances, which needs further analysis.

## 5. Summary

We investigated properties of the nonlinear decay of Alfvén waves in the solar wind taking into account the joint action of both scalar- and vector-type nonlinear interactions among Alfvén and slow waves. This study extends and complements previous studies by Zhao et al. (2014, 2015a) in which scalar- and vector-type nonlinearities have been investigated separately in two opposite wavelength limits. The most important new properties of the decay and their consequences are summarized as follows:

1. The transition from the 2D scalar to 3D vector decay is smooth and occurs in the extended wavenumber range  $10^{-4} \lesssim \rho_i k_{0\perp} \lesssim 10^{-3}$ . The mean value of the transition wavenumber  $\rho_i k_{tr} \approx 5 \times 10^{-4}$  is thus much smaller than the transition wavenumber  $\rho_i k_{tr} \approx 10^{-2}$  found by Zhao et al. (2015a) from comparison of separate scalar and vector decays. This numerical result exhibits importance of the joint action of scalar and vector nonlinear interactions, reducing the transition wavenumbers.

2. In application to the solar wind, it means that the vast majority of Alfvén waves in the extended range  $10^{-4} \lesssim \rho_i k_{0\perp} \lesssim 1$  are affected by the vector nonlinear interaction. The Alfvénic decay is thus 3D over almost four decades of scales below the ion gyroscale. The decay is essentially nonlocal in this range, introducing a nonlocal spectral transport of wave energy across several decades from MHD scales directly to the ion kinetic scales  $\rho_i k_{1\perp} \sim 1$ .

3. Because of the decay nonlocality, the MHD Alfvén waves with  $5 \times 10^{-4} \lesssim \rho_i k_{0\perp} < 10^{-1}$  propagating from the Sun cannot generate counter-propagating Alfvén waves with similar scales needed for the turbulent cascade. Only Alfvén waves of the largest scales (at least  $\rho_i k_{0\perp} \sim 10^{-4}$ ) can generate the seed counter-propagating waves initiating the turbulent cascade.

4. Evaluation of the nonlinear frequency shift shows that the product Alfvén waves can still be approximately described as the normal Alfvén eigenmodes. On the contrary, the nonlinearly driven slow waves deviate considerably from the normal modes and therefore are difficult to identify on the basis of their phase velocities and/or polarization.

5. A new range of unstable highly oblique product waves arises at ion kinetic scales due to the joint action of scalar and vector nonlinearities.

2. Another general trend observed in Figures 1, 3, and 4 for all three channels (except for Channel I at the lowest wavenumbers  $\rho_i k_{0\perp} \sim 10^{-4}$ ) is the nonlocal character of the Alfvén wave decay not only in the wavenumber  $k_{1\perp}$  but also in the azimuthal angle  $\theta$ . This makes the wave spectrum azimuthally symmetric.

Influence of wave and plasma parameters on the decay, such as the wave amplitude and frequency, plasma  $\beta_i$ , and temperature ratio  $T_e/T_i$  is also investigated. The nonlinear

growth rate normally increases with larger initial amplitude, smaller initial frequency, and smaller  $\beta_i$ . At larger  $T_e/T_i$ , the normalized growth rate is larger in the strongest channel: Channel I. Furthermore, our results revealed the following decay properties in three possible decay channels in the solar wind.

*Channel I.* In this channel the decay is usually strongest. At the largest scales  $\rho_i k_{0\perp} \lesssim 10^{-4}$  the decay of MHD Alfvén waves is 2D, generating a broadband wavenumber range of product waves with collinear perpendicular wavevectors  $\mathbf{k}_{1\perp} \parallel \mathbf{k}_{2\perp} \parallel \mathbf{k}_{0\perp}$ . At still very small MHD wavenumbers around  $\rho_i k_{0\perp} \sim 5 \times 10^{-4}$ , the Channel I decay is driven by the competing scalar and vector nonlinear interaction and becomes 3D. The 3D decay of MHD Alfvén waves, dominating at  $\rho_i k_{0\perp} > 10^{-3}$ , is nonlocal and generates kinetic-scale product waves with  $\rho k_\perp \approx 0.5$  and  $\theta \approx \pm 45^\circ$ .

*Channel II.* At  $\rho_i k_{0\perp} > 10^{-4}$ , the decay in this channel is entirely 3D and nonlocal, generating kinetic-scale Alfvén waves with two peaks in the wavenumber spectrum,  $\rho_i k_\perp \approx 0.5$  and  $\rho_i k_\perp \approx 10$ , and two peaks in the azimuthal angle spectrum,  $\theta \approx 45^\circ$ . The kinetic-scale pump Alfvén waves with  $\rho_i k_{0\perp} \sim 0.5$  generates product waves with similar wavenumbers, but they are rather spread in the azimuthal angle,  $45^\circ \leq |\theta| \leq 90^\circ$ .

*Channel III.* Only kinetic-scale Alfvén waves with  $\rho_i k_{0\perp} \sim 1$  can decay in this channel, The decay here is 3D and local in wavenumber space, exciting product waves at the same scales but nonlocal in the azimuthal angle with two peaks at  $\theta \sim \pm 45^\circ$ .

It should be noted that counter-propagating Alfvén waves can undergo strong incoherent interactions governing the turbulence of Alfvén waves (e.g., Goldreich & Sridhar 1995; Schekochihin et al. 2009). Generation of Alfvénic turbulence has been observed in recent 2D and 3D hybrid particle-in-cell simulations (e.g., Franci et al. 2015a, 2015b, 2018), where spectra of electric and magnetic fields, velocity, and density exhibited power-law dependences in the wide wavenumber range from MHD to subproton scales. For MHD Alfvén waves propagating in the same direction, the previous hybrid simulations have confirmed the existence of the nonlinear decay (e.g., Matteini et al. 2010a, 2010b; Lin et al. 2012). These simulations indicate that the nonlinear evolution of copropagating Alfvén waves is controlled by the resonant three-wave interactions between Alfvén and slow waves, while the nonlinear evolution of counter-propagating Alfvén waves is dominated by the strong nonresonant interactions among Alfvén waves. Therefore, the Alfvén decay instability is preferred in the inner solar wind (e.g., Tenerani & Velli 2013), particularly in the fast streams where the overwhelming majority of Alfvén waves propagate away from the Sun.

Our theoretical analysis assumes the homogeneous plasma density and magnetic field. However, as the solar wind is radially expanding, its density and magnetic field depend on the heliocentric distance. The expansion effects in the nonlinear decay of Alfvén waves have been studied by Matteini et al. (2010a, 2010b), Matteini et al. (2012), Tenerani & Velli (2013), and Del Zanna et al. (2015). Because the pump Alfvén wave amplitude decreases with the radial distance, the decay rate is, in general, reduced (e.g., Tenerani & Velli 2013, and Del Zanna et al. 2015). Therefore, in order to account for the radial evolution of the 3D decay of the Alfvén wave, one needs

to include the expansion effects in a two-fluid plasma model, which is a task for future studies.

This research was supported by NSFC under grant No. 11673069, No. 41531071, and No. 11303099, by NSF of Jiangsu Province under grant No. BK20161617. Y.V. and J.D.K. acknowledge support from the Belgian Science Policy Office through Prodex/Cluster PEA 90316, Prodex/THOR-CSW PEA 4000116805, and IAP Programme project P7/08 CHARM. J.S.Z. especially acknowledges support from the Youth Innovation Promotion Association CAS, and from Key Laboratory of Solar Activity at NAO, CAS, under grant No. KLSA201714.

### ORCID iDs

J. S. Zhao  <https://orcid.org/0000-0002-3859-6394>  
 Y. Voitenko  <https://orcid.org/0000-0002-4139-1795>  
 J. De Keyser  <https://orcid.org/0000-0003-4805-5695>  
 D. J. Wu  <https://orcid.org/0000-0003-2418-5508>

### References

- Araneda, J. A., Marsch, E., & Vinas, A. F. 2007, *JGR*, **112**, A04104  
 Asgari-Targhi, M., van Ballegoijen, A. A., Cranmer, S. R., & DeLuca, E. E. 2013, *ApJ*, **773**, 111  
 Bale, S. D., Kellogg, P. J., Mozer, F. S., Horbury, T. S., & Reme, H. 2005, *PhRvL*, **94**, 215002  
 Barnes, A., & Hollweg, J. V. 1974, *JGR*, **79**, 2302  
 Bavassano, B., Pietropaolo, E., & Bruno, R. 2000, *JGR*, **105**, 15959  
 Bemporad, A., & Abbo, L. 2012, *ApJ*, **751**, 110  
 Canals, A., Breen, A. R., Ofman, L., Moran, P. J., & Fallows, R. A. 2002, *AnGeo*, **20**, 1265  
 Cohen, R. H., & Kulsrud, R. M. 1974, *PhFl*, **17**, 2215  
 Cranmer, S. R., & van Ballegoijen, A. A. 2005, *ApJ*, **156**, 265  
 Del Zanna, L. 2001, *GeoRL*, **28**, 2585  
 Del Zanna, L., Matteini, L., Landi, S., et al. 2015, *JPIPh*, **81**, 3202  
 Del Zanna, L., Velli, M., & Londrillo, P. 2001, *A&A*, **367**, 705  
 Derby, N. F., Jr 1978, *ApJ*, **224**, 1013  
 Franci, L., Landi, S., Matteini, L., Verdini, A., & Hellinger, P. 2015a, *ApJ*, **812**, 21  
 Franci, L., Landi, S., Verdini, A., Matteini, L., & Hellinger, P. 2018, *ApJ*, **853**, 26  
 Franci, L., Verdini, A., Matteini, L., Landi, S., & Hellinger, P. 2015b, *ApJL*, **804**, L39  
 Galeev, A. A., & Oraevskii, V. N. 1963, *SPHD*, **7**, 988  
 Goldreich, P., & Sridhar, S. 1995, *ApJ*, **438**, 763  
 Goldstein, M. L. 1978, *ApJ*, **219**, 700  
 Goossens, M., Erdelyi, R., & Ruderman, M. S. 2011, *SSRv*, **158**, 289  
 Hahn, M., Landi, E., & Savin, D. W. 2012, *ApJ*, **753**, 36  
 Hasegawa, A., & Chen, L. 1976, *PhRvL*, **36**, 1362  
 He, J., Pei, Z., Wang, L., et al. 2015a, *ApJ*, **805**, 176  
 He, J., Tu, C., Marsch, E., et al. 2015b, *ApJL*, **813**, L30  
 Heyvaerts, J., & Priest, E. R. 1983, *A&A*, **117**, 220  
 Isobe, H., Proctor, M. R. E., & Weiss, N. O. 2008, *ApJL*, **679**, L57  
 Jayanti, V., & Hollweg, J. V. 1993, *JGR*, **98**, 19049  
 Leamon, R. J., Smith, C. W., Ness, N. F., Matthaeus, W. H., & Wong, H. K. 1998, *JGR*, **103**, 4775  
 Li, H., Wang, C., Belcher, J. W., He, J., & Richardson, J. D. 2016a, *ApJL*, **824**, L2  
 Li, H., Wang, C., Chao, J. K., & Hsieh, W. C. 2016b, *JGR*, **121**, 42  
 Lin, Y., Johnson, J. R., & Wang, X. Y. 2012, *PhRvL*, **109**, 125003  
 Maneva, Y. G., Vinas, A. F., Moya, P. S., Wicks, R. T., & Poedts, S. 2015, *ApJ*, **814**, 33  
 Matsumoto, T., & Suzuki, T. K. 2012, *ApJ*, **749**, 8  
 Matteini, L., Hellinger, P., Landi, S., Travnicek, P., & Velli, M. 2012, *SSRv*, **172**, 373  
 Matteini, L., Landi, S., Del Zanna, L., Velli, M., & Hellinger, P. 2010a, *GeoRL*, **37**, L20101  
 Matteini, L., Landi, S., Velli, M., & Hellinger, P. 2010b, in *AIP Conf. Proc.* 1216, Twelfth International Solar Wind Conference, ed. M. Maksimovic et al. (Melville, NY: AIP), 223  
 Matthaeus, W. H., Zank, G. P., Oughton, S., Mullan, D. J., & Dmitruk, P. 1999, *ApJL*, **523**, L93  
 McIntosh, S. W., de Pontieu, B., Carlsson, M., et al. 2011, *Natur*, **475**, 477  
 McKenzie, J. F., Banaszkiewicz, M., & Axford, W. I. 1995, *A&A*, **303**, L45  
 McLaughlin, J. A., De Moortel, I., & Hood, A. W. 2011, *A&A*, **527**, A149  
 Miyamoto, M., Imamura, T., Tokumaru, M., et al. 2014, *ApJ*, **797**, 51  
 Morton, R. J., Tomczyk, S., & Pinto, R. 2015, *NatCo*, **6**, 7813  
 Narita, Y., & Marsch, E. 2015, *ApJ*, **805**, 24  
 Nariyuki, Y., Hada, T., & Tsubouchi, K. 2014, *ApJ*, **793**, 138  
 Nishikawa, K. 1968, *JPSJ*, **24**, 916  
 Roberts, O. W., Li, X., & Jeska, L. 2015, *ApJ*, **802**, 2  
 Roberts, O. W., Narita, Y., Li, X., Escoubet, C. P., & Laakso, H. 2017, *JGR*, **122**, 6940  
 Schekochihin, A., Cowley, S., Dorland, W., et al. 2009, *ApJS*, **182**, 310  
 Shi, M., Li, H., Xiao, C., & Wang, X. 2017, *ApJ*, **842**, 63  
 Shi, M. J., Xiao, C. J., Li, Q. S., et al. 2015, *ApJ*, **815**, 122  
 Shoda, M., & Yokoyama, T. 2016, *ApJ*, **820**, 123  
 Suzuki, T., & Inutsuka, S. 2005, *ApJL*, **632**, L49  
 Suzuki, T., & Inutsuka, S. 2006, *JGR*, **111**, A06101  
 TenBarge, J. M., Howes, G. G., & Dorland, W. 2013, *ApJ*, **774**, 139  
 Tenerani, A., & Velli, M. 2013, *JGRA*, **118**, 7507  
 Terasawa, T., Hoshino, M., Sakai, J. I., & Hada, T. 1986, *JGR*, **91**, 4171  
 van Ballegoijen, A. A., & Asgari-Targhi, M. 2016, *ApJ*, **821**, 106  
 Vasquez, B. J., & Hollweg, J. V. 1996, *JGR*, **101**, 13527  
 Verdini, A., & Velli, M. 2007, *ApJ*, **662**, 669  
 Voitenko, Y., & De Keyser, J. 2011, *NPGeo*, **18**, 587  
 Voitenko, Y., & Goossens, M. 2004, *NPGeo*, **11**, 535  
 Voitenko, Y., & Goossens, M. 2005, *JGR*, **110**, A10S10  
 Yang, L., Lee, L. C., Chao, J. K., et al. 2016, *ApJ*, **817**, 178  
 Zhao, J. S., Voitenko, Y., De Keyser, J., & Wu, D. J. 2015a, *ApJ*, **799**, 222  
 Zhao, J. S., Voitenko, Y., Guo, Y., Su, J. T., & Wu, D. J. 2015b, *ApJ*, **811**, 88  
 Zhao, J. S., Voitenko, Y., Wu, D. J., & De Keyser, J. 2014, *ApJ*, **785**, 139  
 Zhao, J. S., Wu, D. J., & Lu, J. Y. 2013, *ApJ*, **767**, 109